IOP Publishing 2D Mater. 13 (2026) 015018 https://doi.org/10.1088/2053-1583/ae2522

2D Materials

RECEIVED
1 July 2025

REVISED
18 November 2025

ACCEPTED FOR PUBLICATION
27 November 2025

PUBLISHED
10 December 2025

PAPER

Sliding-induced topological transitions in bilayer biphenylene

L L Lage[1], S Bravo[2], O Arroyo-Gascón[3], Leonor Chico[4] and Andrea Latgé[1,*]

[1] Instituto de Física, Universidade Federal Fluminense, Av. Litorânea sn, Niteroi 24210-340, RJ, Brazil
[2] Departamento de Física, Universidad Técnica Federico Santa María, Casilla 110-V, Valparaíso, Chile
[3] Nanotechnology Group, USAL-Nanolab, University of Salamanca, Salamanca 37008, Spain
[4] GISC, Departamento de Física de Materiales, Facultad de Ciencias Físicas, Universidad Complutense de Madrid, Plaza de las Ciencias 1, 28040 Madrid, Spain
[*] Author to whom any correspondence should be addressed.

E-mail: alatge@id.uff.br

Keywords: biphenylene, topology, Lifshitz transition, type II Dirac cones

Supplementary material for this article is available online

Abstract

The complex geometry of biphenylene materials offers alternative routes for exploring novel stacking configurations achieved by piling up carbon-thin sheets. Here we investigate sliding-induced topological transitions in biphenylene bilayers, proposing various novel stacking configurations. They are analyzed from a symmetry perspective and described in detail, highlighting the intricate patterns of type-II Dirac cone crossings. Topological changes in the Fermi surface are assessed via the Euler characteristic, linking each transition to its corresponding symmetry, which can be experimentally tested by conductance measurements. Moreover, the ability to tune these topological properties by sliding the layers provides a simpler and more effective way to observe such phenomena.

1. Introduction

The biphenylene network (BPN) is a promising two-dimensional (2D) material that was predicted long ago [1] and has experienced a revitalization due to its unique structural and electronic properties [2]. Recently, it has gained significant attention mainly due to its experimental synthesis based on on-surface interpolymer dehydrofluorination polymerization protocols [3, 4]. As a derivative of biphenyl, biphenylene consists of two hexagonal carbon rings connected directly by two carbon-carbon double bonds in a linear arrangement, resulting in a planar sp^2 structure that combines six-fold, eight-fold, and four-fold carbon rings (see figure 1(a)). Being a new carbon allotrope related to graphene but with a mixed geometry [5], it possesses distinct electronic properties and symmetries. In particular, its band structure shows a type-II Dirac cone near the Fermi energy, with carrier velocities of the same sign and anisotropic transport properties [6]. These features have been proposed to be of interest for nanoelectronics [7, 8]. The electronic stability of one-dimensional biphenylene systems was also studied before its synthesis using first-principles calculations, including ribbons and tubes of different widths and morphologies [2]. Biphenylene-based materials stand out among 2D systems due to their unique topology and electronic properties. Unlike graphene, which is gapless and exhibits an isotropic Dirac dispersion, biphenylene displays type-II Dirac cones and can host highly anisotropic electronic and transport properties, offering new opportunities for band engineering. In comparison to transition metal dichalcogenides (TMDs), which are semiconductors with relatively rigid band structures, BPNs exhibit tunable electronic responses via stacking, sliding, and strain. Moreover, being composed entirely of carbon. The combination of structural novelty, electronic richness, and chemical simplicity positions biphenylene as a compelling alternative to more conventional 2D materials.

Because of the complex geometry of biphenylene, novel stacking configurations may be achieved by piling up such carbon-thin sheets. In a recent work [9], we proposed new symmetric bilayer stackings with

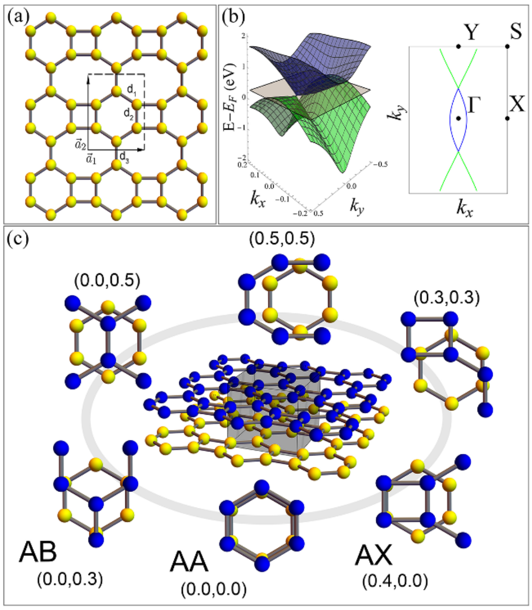

Figure 1. (a) Biphenylene monolayer structure with bond lengths $d_1 = 1.41$ Å, $d_2 = 1.45$ Å, and $d_3 = 1.46$ Å. (b) Type-II band structure of BPN monolayer with Dirac points at $E = 0.26$ eV; valence (green) and conduction (blue) bands are shown. (c) Bilayer stacking configurations labeled (δ_x, δ_y).

different electronic properties. Similarly to graphite, these bilayers are held together by van der Waals (vdW) forces. In bilayer graphene, the two primary stacking arrangements of interest are AA and AB (Bernal), with different Dirac cone patterns, namely, four linear crossings or touching parabolas, respectively, at the Fermi level. By introducing a gate voltage between the layers, in the AB case a band gap can be achieved [10]. Trigonal warping effects also modify the parabolic dispersion, with the appearance of sets of Dirac-like linear bands [11]. For bilayer biphenylene, in contrast to the monolayer, the lower-energy type-II Dirac cone in the conduction band is split. In the AA case, this splitting gives rise to two cones, so that one of them is actually very close to the Fermi level. Each of these cones has two branches with velocities of the same sign and dissimilar magnitude, in contrast to the isotropic behavior of Dirac cones in graphene [9].

Another way to tune the band structure properties of monolayer biphenylene is by means of strain: in addition to modifying the position of the Dirac cone, the Fermi surface characteristics can be altered, as recently shown [12]. In fact, the Fermi surface is a fundamental feature in understanding the electronic topology of a system. At some critical points, the band connectivity can change abruptly, as observed by Lifshitz long ago [13]. To detect such electronic topological transition, known as a Lifshitz transition [14], the Fermi level can be adjusted to the exact place in the band structure where the topological shift occurs. However, in general, its experimental implementation involves large variations in electron density by doping or by applying high pressure or magnetic fields [15–19]. The rise of low-dimensional materials has allowed for sizable modifications of such characteristics via strain. These changes can include the splitting or merging of Fermi surface pockets of monolayer and bilayer systems [16, 20, 21] and have been experimentally observed in the electronic bands of graphene [17, 22]. Topological transitions could dramatically change the physical properties of the materials, such as thermoelectric and transport responses [23]. In fact, applied in-plane strain or displacements between layers in graphene bilayer systems may also change the topology of the Dirac cones [16, 21, 24]. In addition, the topological properties of the graphene-based bilayer can be adjusted by sliding [21] and twisting [25–27] their layers, which has opened an avenue for the so-called slidetronics, in the context of ferroelectric materials, twistronics [28–30] and spintronics in graphene-based systems, where the exchange proximity interaction in bilayer graphene can be explored for electrical spin manipulation [31]. Moreover, BPNs have been theoretically predicted to exhibit anisotropic spin responses [32, 33]. While, to the best of our knowledge, there are not any experimental reports regarding such properties for BPN, in type-II Dirac and Weyl semimetals there are experimental works showing an anisotropic behavior in transport measurements attributed to the type-II cones present in these materials [34, 35]. Recent advances in electron microscope tip technology now allow precise manipulation of thin material layers, with high angular control, as demonstrated in twisted bilayer systems [36], using orientational displacement by assembled heterostructures placed on nanoridge arrays [37], and adopting Kelvin probe force microscopy techniques [38, 39]. Beyond rotation, these techniques also enable controlled sliding of isolated thin films, extending stacking-engineering approaches to a variety of materials. The use of sliding engineering techniques avoids the difficulties of traditional methods in obtaining topological transitions, such as chemical doping or strain engineering, which often introduce defects or require complex sample fabrication [40, 41]. This points to the exploration of similar mechanisms for biphenylene-based systems.

Here, we propose novel bilayer configurations by continuously sliding one BPN layer over the other. We have found that such new stackings may have different band structures with respect to the split Dirac cones. Additionally, we have identified several Lifshitz transitions induced by sliding, which are allowed without externally breaking the crystal symmetries or doping the material. To investigate changes in the band structure and Fermi surface topology related to these transitions, we have performed first-principles density functional theory (DFT) calculations, as detailed in the next section. Since spin–orbit effects are negligible (of the order of meV) compared to typical hopping parameters (of the order of eV) in biphenylene systems, the effect is not included in the following computations, as previously discussed [9]. DFT calculations of monolayer biphenylene reveal a type-II Dirac cone with electron- and hole-like pockets [42] for a surface cutting the Dirac nodes, as shown in figure 1(b). Moreover, Dirac nodes do not occur at high symmetry points, as also reported for bidimensional TMDs such as WTe_2 and $MoTe_2$ [43]. A tight-binding description fitting quite well with our DFT results is also discussed in appendix.

Because the studied bilayer BPNs of different stacking profiles exhibit metallic properties, we must choose a topological invariant capable of capturing a topological transition, since it is not possible to directly observe a usual insulating topological transition from the corresponding band structures. We use the Euler characteristic as a topological invariant to analyze the Fermi sea of different stacking configurations. Changes in the Fermi surface can be probed by different experimental techniques such as angle-resolved photoemission spectroscopy [44–46], magnetotransport [47, 48] and scanning tunneling spectroscopy [49]. However, a clear connection between experimentally measurable physical quantities and the Euler characteristic remains lacking in the literature. In this line, a theoretical physical quantity was recently proposed by Tam *et al* [50] that should be understood via experimental transport measurements. Our findings show distinct behaviors depending on their symmetry, which we call high-symmetry stacking (HSS) and low-symmetry stacking (LSS). In the case of the LSS set, the invariant does not discriminate between different sliding configurations, since all yield a null invariant.

2. Computational details

DFT calculations were carried out using the Quantum ESPRESSO software [51, 52] within the generalized gradient approximation and the Perdew–Burke–Ernzerhof exchange correlation functional [53]. In a first stage, a relaxation process was performed starting with the stacking of $(0.0, 0.0)$. To achieve the other stackings, rigid displacements were used for the in-plane coordinates, simulating a clamp to obtain the desired sliding step. The out-of-plane coordinate was allowed to relax in order to minimize with a variable cell configuration. The force tolerance along the vertical direction was set to $0.01\,\mathrm{eV\,Å^{-1}}$. After the relaxation stage, the electronic structure was obtained for each stacking, using an energy cutoff of 100 Ry, along with a tolerance of 10^{-9} eV and a norm-conserving pseudo-potential [54]. In addition, a Monkhorst–Pack grid in momentum space with $10 \times 12 \times 1$ points was used, which yields well-converged results in all cases. To ensure an accurate description of the layered system all the calculations have included a correction for long-range vdW forces using the Grimme-DFT-D3 method with zero damping, as implemented in the Quantum ESPRESSO package [55]. To verify dynamical stability we have calculated phonon dispersion calculations for representative stackings. The phonons computation was performed for the HSS using the phonopy package [56] and adopting a $5 \times 5 \times 1$ supercell; the results shown in the SM [57] certify that the proposed stackings are mechanically stable.

To obtain the 2D Fermi surfaces, an additional non self-consistent calculation was performed for each stacking using the output results of the previous electronic structure calculations. The only change in this step is the use of a denser M–K grid with $50 \times 60 \times 1$ points. This finer calculation is then used to interpolate the bands of each stacking using Fourier interpolation approach, implemented in the BoltzTrap2 package [58]. An interpolation with 3 additional points for each interval was used in the previous (non self-consistent) grid. The interpolated bands are finally post-processed to obtain the contours at the Fermi level. The irreducible representations of the band structures are obtained by using the IrRep code [59].

3. Results & discussions

3.1. System geometries and symmetries

The geometry of monolayer biphenylene is shown in the left panel of figure 1(a). The periodicity of the system is described by a rectangular unit cell in the xy plane, centered on the hexagonal ring. Repetition of this pattern creates octagonal rings and four-atom rings. The relaxed unit cell vectors $\vec{a}_1 = 3.76\ \hat{x}$ and $\vec{a}_2 = 4.52\ \hat{y}$ are also shown in the figure. The mean interlayer distance ($\bar{d}_\perp$) obtained by the relaxed structures within vdW-DFT, averaged over all the stackings is $\bar{d}_\perp = 3.492$ Å, where the minimum and maximum values are, respectively, 3.393 Å and 3.548 Å. The complete table for all studied stackings is included in the SM [57] The three inner-layer distances are the same for all bilayers, $d_1 = 1.41$ Å, $d_2 = 1.45$ Å, and $d_3 = 1.46$ Å, which also coincide with those of the monolayer, indicated in figure 1(a). The corresponding Brillouin zone (BZ) is depicted in the right panel (figure 1(b)), showing the labels of the high-symmetry points, along with a constant energy cut which contains the type-II Dirac points.

When bilayers are formed, diverse stacking possibilities emerge. This freedom is ultimately restricted by physical and chemical properties that establish the most favorable configurations to be realized experimentally. In later sections we will comment on the stability and energetic landscape that the different stackings comprise, but for the sake of symmetry analysis, we focus here on the relative spatial orientation of the atomic sites and their space group (SG) classification.

The coupling of two biphenylene monolayers can be performed following different geometric configurations. First, we restrict the set of stackings in which rotational symmetries play a role. Thus, we discard all stackings with the trivial SG P1 (No. 1). We classify the remaining stackings into two main sets, introducing a useful notation.

Figure 1(c) presents some of the stackings studied in this work (more configurations are detailed in the SM [57] figure S1). The stackings are depicted by showing the hexagonal ring of the bottom layer (yellow atoms) and the six atoms on the top layer (blue atoms) within the unit cell. To generically describe the relative sliding, we fix the bottom biphenylene layer and translate the upper one. We assume that the starting position of the upper layer is the one where the in-plane atomic coordinates coincide with the in-plane atomic coordinates of the bottom layer, i.e. direct or AA stacking. Rigid translations are described by a vector $\boldsymbol{\delta} = (\delta_x, \delta_y)$ in the xy plane whose Cartesian components quantify the amount of displacement in fractions of the respective lattice vectors, so that δ_x and δ_y can take values from 0 to 1. It is important to note that the sliding can be described in this form because the same rectangular unit cell (with 12 atoms) can be maintained throughout the process.

The three stackings shown in figure 1(c), denoted AA [60], AX, and AB, were reported by us in a previous work [9]. In this work we explore the continuum of geometries obtained by smoothly sliding one biphenylene layer on top of the other. As an example of the novel systems studied here, the three cases depicted in the upper part of the panel are analyzed here for the first time. All the bilayers are identified in figure 1(c) with their corresponding coordinates (δ_x, δ_y). Using this vector notation, two sets of stackings can be described. Starting the sliding process at $\boldsymbol{\delta} = (0, 0)$, we find three possible routes with non-trivial rotational symmetries. We can follow the lines $(\mu, 0)$ and $(0, \mu)$, or the diagonal line (μ, μ), with μ ranging from 0 to 1. For simplicity, we allow μ to take values only from 0 to 0.5, since the other quadrants of the (δ_x, δ_y) plane are obtained by symmetry considerations.

First, we focus on four possible stacking configurations with the maximal number of symmetries that biphenylene bilayers can have, namely eight. This HSS set comprises the $(0.0, 0.0)$, $(0.5, 0.0)$, $(0.0, 0.5)$, and $(0.5, 0.5)$ geometries. All rotational symmetries of the HSS set can be connected to the point group mmm (D_{2h}), the same as in the HSS set that generates the monolayer SG. The difference among the SGs of the HSS set is that for the stackings $(0.5, 0.0)$, $(0.0, 0.5)$ and $(0.5, 0.5)$, some of the rotational symmetries become nonsymmorphic. In particular, for $(0.5, 0.0)$ and $(0.0, 0.5)$ stackings, four of the eight symmetries become nonsymmorphic with a fractional translation vector equal to the corresponding sliding vector. In the case of the $(0.5, 0.5)$ stacking, four symmetries also become nonsymmorphic, but now the fractional translation vector has both nonzero components. In summary, with respect to the HSS set, the $(0.0, 0.0)$ stacking is characterized by the SG Pmmm (No. 47), the $(0.5, 0.0)$, $(0.0, 0.5)$ stackings by SG Pmma (No. 51), and finally the $(0.5, 0.5)$ stacking by SG Pmmn (No. 59). The LSS set is composed of configurations $(\mu, 0)$, $(0, \mu)$ and (μ, μ) [with $\mu \in (0.0, 0.5)$], as well as two additional lines with rotational symmetries which arise by fixing one of the components of the $\boldsymbol{\delta}$ vector to 0.5 and varying the other component, i.e. $(\mu, 0.5)$, $(0.5, \mu)$. For this set, the classification is also straightforward. When we move along the $(\mu, 0)$, $(0, \mu)$ lines we break four symmetries; only spatial inversion, a rotation, and a mirror plane, both with respect to the axis in which the sliding occurs, are preserved. This yields SG P2/m (No. 10) for both sliding lines. In the case of the $(\mu, 0.5)$, $(0.5, \mu)$ lines, the number of rotational symmetries is the same as in the previous cases, but with nonsymmorphic rotation and mirror symmetries. This yields SG P2_1/m (No. 11) for both lines. Finally, diagonal sliding breaks all symmetries with the exception of spatial inversion, resulting in SG P$\bar{1}$ for the (μ, μ) line. The relation between the symmetry and the geometry of the different sliding configurations with respect to the layer displacements δ_x and δ_y is graphically summarized in a chessboard-like diagram in figure 2. Each bilayer configuration belongs to a SG that may change with displacement. The symmetry of the bilayers is visually represented by the color of the squares composing the diagram. We show in the following that the diversity of symmetries presented by the BPN bilayers is closely related to their different band structures. Moreover, the band crossing and anticrossings at the type-II Dirac cones along the Y–Γ path present three possibilities; four crossing bands, two crossing bands and two types of anticrossing bands. They are represented by circles, stars and triangles, respectively, inside the diagram boxes of figure 2.

3.2. First-principles structural and electronic properties

We perform first-principles calculations for all HSS and for a subset of LSS which correspond to values of $\mu = n/10$ for $n \in \{1, 2, 3, 4\}$. For the bilayer structures studied in this work, the sliding process does not produce substantial structural modifications such as unit cell volume variations or interlayer distance fluctuations.

Figure 3(a) gathers the band structures corresponding to representative cases from the sliding diagram in figure 2. Notice that the complete symmetry information for each sliding configuration is included

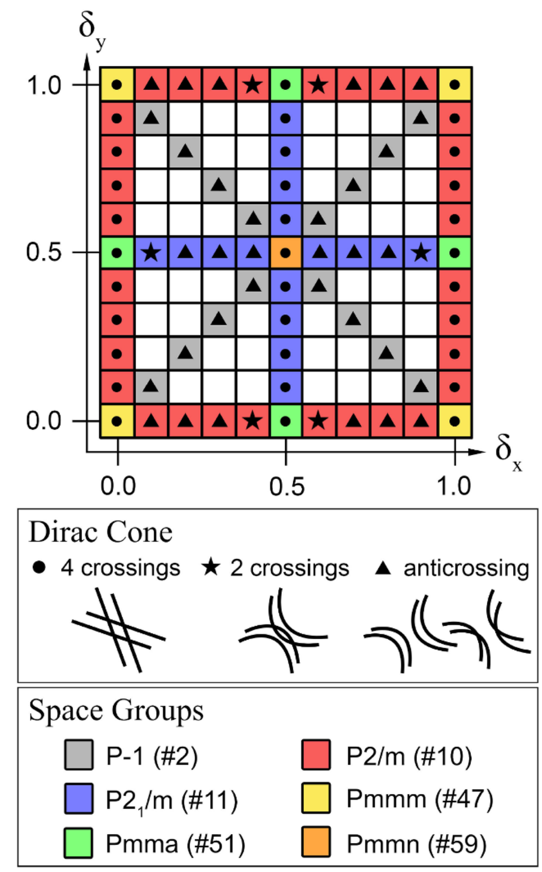

Figure 2. Sliding diagram for the bilayer stackings: classification of the different space groups and Dirac cone patterns with respect to the displacements δ_x and δ_y. Each square of the grid is colored according to the space group of the specific bilayer; the color code is shown in the bottom panel. Inside the square, a symbol indicates the type of band crossing at the double Dirac cone closest to the Fermi energy: circles (4 crossings), stars (2 crossings) and triangles (anticrossing), as indicated in the panel below the diagram.

in the first quadrant region of the diagram, which includes the displacements $0 \leqslant \delta_{x,y} \leqslant 0.5$. Thus, the bands presented in figure 3 are colored according to the SG code for this region of the diagram. Concerning the electronic structure and its dependence on sliding, we start by analyzing the HSS set. The energy bands near the Fermi level for these four stackings are presented in the four corner panels of figure 3(a).

The bands for the direct stacking case AA [(0.0, 0.0); SG No. 47] are presented at the bottom left corner of the figure (yellow curves). The bands are completely split and cross at four points. The two main features discussed are the Dirac nodes and the characteristics associated with the nonsymmorphic symmetries. Considering the latter, the most notable feature due to the joint action of a nonsymmorphic operation and time-reversal symmetry is the formation of nodal lines (NLs) along the boundaries of the BZ; the so-called stick-together bands [61]. The type of NL is related to the type of stacking. Thus, we can see that the case (0.5, 0.0) has a NL along the X–S high-symmetry path, and the case (0.0, 0.5) has a nodal line along Y–S. Both cases correspond to the SG No. 51, and their band structures are shown in green at top-right and bottom-left panels of figure 3(a). As expected, the (0.5, 0.5) bilayer presents a NL along the entire boundary of the BZ. Therefore, the HSS set allows us to study the entire range of boundary NLs. It is important to emphasize that NLs occur along the boundary of the BZ, irrespective whether they are partial NLs or NLs along the whole boundary, with one pair of bands involved in the formation of each NL. Otherwise, Dirac nodes are not related to NLs, since they form in separate regions of the band structure.

The presence of type-II Dirac cones can be directly observed in the band structures. All HSS examples host four cones along the Γ–Y line in reciprocal space. The cones are produced by the crossing of two pairs of bands with large magnitude of the velocity with another pair with much smaller velocities. Each pair stems from the bilayer splitting. The location of the crossings is modified by varying the stacking: the (0.5, 0.0) and (0.0, 0.5) cases present a very close pair of Dirac cones while the other two configurations have a higher separation between the cones. In terms of reciprocal space symmetry, the superposition of the bands actually entails crossovers by analyzing the irreducible representations of the bands along the Γ–Y line. From a DFT-based group theory analysis [59, 62, 63], the symmetry along this line is described by the point group isomorphic to mm2 (C_{2v}) with four elements. This is true for all the HSSs, and implies that there are four irreducible representations describing the symmetry of the bands in this region.

We study the symmetry of the bands along Γ–Y (the so-called Δ line) at different locations, and present the results in figure 3(b), for the representative HSS (0.0, 0.0) and LSS (0.2, 0.0) geometries. For the HSS case, the irreducible representations of the bands that meet at each of the nodes are different, and thus cannot mix, indicating that they can only cross. This implies that these crossings are strict Dirac points. Now we turn to the LSS. We focus on the subset of lines $(\mu, 0)$ and $(0, \mu)$ (red bands in figure 3), since the lines $(\mu, 0.5)$ and $(0.5, \mu)$ (blue bands) behave similarly. Additional bands for these two lines are also presented in figure S3–S4 of the SM [57], where the first row is for specific values on the $(\mu, 0)$ line and the second row represents the cases for the $(0, \mu)$ line. In general terms, moving away from the HSS set, the momentum-space symmetries are reduced along the Δ line, decreasing the number of available irreps to only two. Therefore, there are fewer possibilities to form four simultaneous Dirac nodes. Namely, four nodes are possible only if the pairs of crossing bands transform under different irreps. If each pair of bands with different velocities

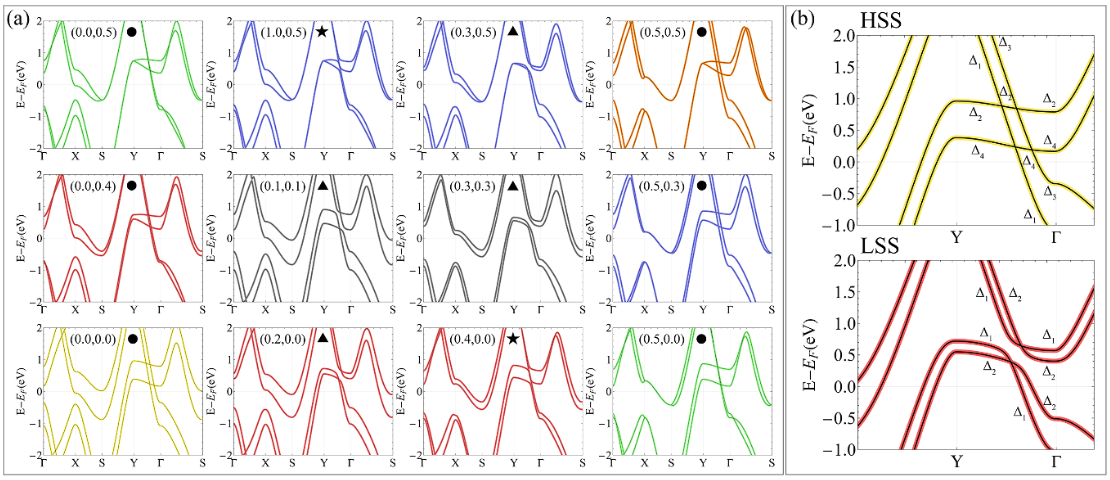

Figure 3. (a) Band structures for the biphenylene bilayers corresponding to the displacements (δ_x, δ_y). Symbols and colors refer to the diagram of figure 2. (b) Electronic bands along the Y–Γ line exhibiting the four crossings for HSS (0.0, 0.0) and LSS (0.2, 0.0), labeled with the corresponding irreps Δ_i.

has a mixed irrep character, i.e. one irrep coincides and the other is different, then there can be at most two crossings along Δ. All scenarios (four, two, and zero nodes) are schematically represented in the diagram presented in figure 2 and examples of the band structure are shown in figure 3. It can be observed from the diagram that the cases with four crossings occur along the $(0, \mu)$ line. One of these, the $(0.0, 0.0)$ stacking, is shown in the upper panel of figure 3(b). All the irreps of the bands at the double Dirac cone are different, so they actually cross. This irrep configuration is respected along the entire $(0, \mu)$ line, which explains the robustness of the four Dirac crossings along it.

A different scenario appears along the $(\mu, 0)$ line, where, due to the order of the irreducible representations, the bands at first do not cross and from approximately $\mu = 0.3$ two crossings appear (see figure 3(a) and figure S3 in SM [57]). The anticrossing behavior can be understood by resorting to the lower panel of figure 3(b), which corresponds to the $(0.2, 0.0)$ stacking. The pair of bands with higher velocity have irreps Δ_1 and Δ_2, the same as the pair of bands with lower velocity. Due to the ordering of the bands, they are forced to anticross, so the Dirac cone is gapped. If the irrep order of one pair of bands at the Dirac point were swapped, crossing would be allowed.

These crossings remain robust until the HSS $(0.5, 0.0)$ is reached. This exhausts all possible arrangements of crossings in these bilayers. The behavior on this line makes it clear that the appearance of Dirac nodes is not enforced by symmetry, but only allowed by the underlying group structure. In fact, we have shown that the node formation is highly dependent on the irrep ordering, which is ultimately linked to the energetic properties of stackings. For the case of the diagonal line (μ, μ), the symmetry analysis shows that along the Δ line the symmetry is reduced to the trivial group, and thereby only one type of irrep is possible. Examples of bands corresponding to (μ, μ) stacking are presented in the central panels (black lines) of figure 3 and detailed in figure S5 in the SM [57]. Therefore, no crossings are allowed along this line, hindering the Dirac node formation. The symmetry of the stacked crystal is responsible for changing the dispersion of the bands for the whole electronic levels. In the following we discuss about the Fermi topology regarding only the Fermi level $E = E_F$ as required for this analysis.

Table 1. Summary of Euler characteristics for the Fermi surface topologies presented in figures 4(a)–(d).

Stacking	Blue curves (e-like)	Red curves (h-like)	Total χ
(0.0, 0.0)	Open loop ($\chi = 0$)	Two loops ($\chi = -1$ each)	-2
(0.5, 0.0)	Two loops ($\chi = -1$ each)	Two loops ($\chi = -1$ each)	-1 [or 0 along $(\mu, 0)$]
(0.0, 0.5)	Open loop ($\chi = 0$)	One connected loop ($\chi = -1$)	-1 [or 0 along $(0, \mu)$]
(0.5, 0.5)	One connected loop ($\chi = +1$)	One connected loop ($\chi = -1$)	0 [also 0 along (μ, μ)]

3.3. Fermi sea topology

The metallic character of all stackings motivates the study of the connection between different configurations. We focus on the topology of the complete Fermi sea and compute the Euler characteristic as a topological invariant. We aim to present a robust response that can have different values for the stackings. The

Euler characteristic is an invariant that describes the global topology of a space [64]. Considering in general the Fermi sea as a disconnected space, which is embedded in the BZ torus, there are several ways to compute this invariant. We follow reference [65] and use the definition valid for 2D systems,

$$\chi = \sum_k (2 - 2g_k - b_k) \ , \tag{1}$$

where k labels each different disconnected component of the Fermi sea, g_k represents the corresponding genus, and b_k denotes the number of its boundaries [65]. In general, the Fermi sea topology includes information from all the bands crossing the Fermi level; these regions can be open or closed loops in the torus that constitutes the BZ. Closed loops give rise to electron or hole pockets around certain regions of the BZ. Only closed loops contribute to the Euler characteristic magnitude; neither open loops nor fully filled or unoccupied bands play a role in the Fermi sea topology.

In the following, we mainly restrict the analysis to the HSS set, although we briefly comment on the results for the LSS set, which yields a null topological invariant. A summary of the computed Euler characteristic is shown in table 1. We start with the $(0.0, 0.0)$ stacking as shown in figure 4(a). An open Fermi loop appears with an electron character (blue solid line) and two closed loops with a hole character (red solid lines). Since the open loop does not contribute to χ and each hole-like closed loop contributes with -1, the total result is $\chi = -2$. The zero value of the open loop (labeled $k = 1$) is obtained by verifying that $g_1 = 0$ and the boundary contribution $b_1 = 2$. Next, each hole-like loop constitutes a separate input for χ, named as $k = 2$ and $k = 3$ components. Their genus values are $g_2 = g_3 = 1$ and $b_2 = b_3 = 1$. Therefore, $k = 2$ and $k = 3$ contribute to χ with -1 each, leading to a total value of $\chi = -2$.

Now we examine the $(0.5, 0.0)$ stacking, as presented in figure 4(b). We note that the aforementioned open loop transitions to a closed loop, and a second closed electron-like loop appears and merges with the initial loops. These two loops are then connected due to the NL formation along the X–S line. In contrast, the hole-like part is still composed of two disconnected loops. The combination of the information from the two types of loops produces a Euler characteristic of $\chi = -1$. This is because the electron-like connected loop contributes with $+1$, and the disconnected hole-like loops contribute with -1 each.

It is worth mentioning that the transitions described above, i.e. moving from open to closed loop and the appearance of the new electron-like loop, occur along the $(\mu, 0.0)$ line. Thus, there is a change in topology in this region, which is characterized by a change in χ. Throughout this region, the hole-like loops are not connected, and thus they contribute separately. The same holds for the electron-like loops. Therefore, the total invariant yields zero $(\chi = 0)$, which is preserved along the entire line, since no additional topological transitions occur. Representative Fermi surfaces graphs for this line and other cases are detailed in the SM [57] in figures S6–S8. Hence, on sliding from the $(0.0, 0.0)$ to the $(0.5, 0.0)$ stacking along $(\mu, 0)$, the sequence of the χ values is $\{-2, 0, -1\}$.

The Fermi surface for the $(0.0, 0.5)$ HSS example is depicted in figure 4(c). On the one hand, the electron-like contours merge in one component, which is an open loop, so it does not contribute to the invariant. On the other hand, the hole-like loops exhibit one connected component due to the emergence of a NL, giving $\chi = -1$. Therefore, the final Euler characteristic of the complete Fermi surface is $\chi = -1$. As in the previous line $(\mu, 0)$, the $(0, \mu)$ line also gives a null value for χ. Here again, the contributions of the electron-like and hole-like components compensate. The results illustrating the behavior along this line are presented in SM [57] at figures S6 and S7. In this way, sliding from the $(0.0, 0.0)$ to the $(0.0, 0.5)$ stacking, along $(0, \mu)$, produces the same sequence of values for χ, $\{-2, 0, -1\}$.

Finally, for the $(0.5, 0.5)$ stacking shown in figure 4(d), mergings occur in both electron and hole-like loops. Thus, there is one connected component in each case; their contributions are canceled, and the Euler characteristic is zero. The topology and Euler characteristic for $(0.5, \mu)$, $(\mu, 0.5)$ can be inferred by analyzing figure S8 in the SM [57].

An important point regarding the application of the invariant to distinguish different stacking phases is related to the change of χ with respect to sliding. The Euler parameter enables us to differentiate between the HSSs $(0.0, 0.0)$, $(0.5, 0.5)$ and the pair $(0.0, 0.5)$, $(0.5, 0.0)$, although it does not distinguish between the last two stackings (both have $\chi = -1$). Sliding towards $(0.5, 0.5)$ χ cannot identify a topological transition related to the change from the LSS lines to this particular HSS, since its value is always zero. This indicates that the intrinsic connectivity of the loops at the Fermi level (considering, for example, nodal structures) is not fully represented in the Fermi sea topology described by χ, although being an useful complementary information.

We may call attention to the fact that apparent crossings in the red contour plots are not exactly along the Γ–Y path, but rather in its neighborhood. We corroborated this observation using first-principles calculations. This is crucial since within that region, the apparent crossings occur at general points of the BZ and should be regarded as accidental crossings. In such cases, the bands involved share the same irreducible representations, which prevent them from actually crossing. NLs are robust as long as their protecting symmetries are maintained. Impurities can affect this robustness in several ways. Nonmagnetic impurities in low concentrations generally preserve time-reversal symmetry and the nonsymmorphic

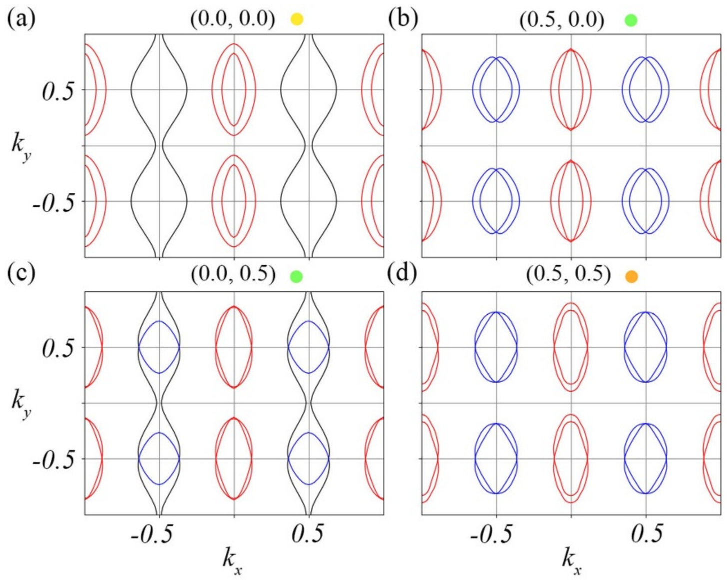

Figure 4. Fermi surface (contour loops) and electronic surface for the HSS set. Blue and red solid lines represent electron-like and hole-like surfaces, respectively. Each stacking is accompanied by the corresponding group symmetry and Dirac cone type as colored circles.

character of the material. However, at higher concentrations, they can form extended states that interfere with or even break the nonsymmorphic crystal symmetry, thus perturbing the NLs. Magnetic impurities, on the other hand, immediately break time-reversal symmetry, which directly lifts a key-protecting symmetry of NLs and destroys their degeneracy. Furthermore, a significant spin–orbit coupling (SOC) within impurity states can also lift NL degeneracies. Both the breaking of time-reversal symmetry and the strong SOC can be induced by placing the material in proximity to other materials, which can affect the NL robustness. The strain is another important perturbation [6, 60]. For the bilayers considered in this work we have lattice anisotropy, and therefore both uniaxial and biaxial strain will preserve the nonsymmorphic symmetries of the NLs. While strain in these cases does not change the fundamental symmetry of the NLs, it can alter their energy location by modifying their dispersion, and affecting the electronic properties of the materials. Moreover, since doping with magnetic impurities produces time-reversal symmetry breaking, in the light of the experimental quantum transport responses measured in magnetic 2D materials [66, 67], we expect that magnetic doping of BPN may have a potential application for spintronic devices.

In summary, the Euler characteristic can be used to distinguish the topological transition of HSS stackings with respect to the LSS. It is worth mentioning that it has been correlated with transport responses related to nonlocal conductance at a planar Josephson junction [68], and with conductance assuming quantized values directly related to the Euler characteristic [69]. This establishes a direct correlation between an experimentally measurable quantity and a subset of our presented HSS phases.

4. Conclusions

In this study, we investigate sliding-induced topological transitions in bilayer biphenylene by exploring different stacking configurations. Through first-principles calculations and symmetry analysis, we demonstrate that the electronic properties of BPN bilayers can be significantly altered by sliding one layer over the other, leading to changes in the topology of the Fermi surface and the emergence of type-II Dirac cones. We explore the electronic and topological properties of a continuum of novel bilayer biphenylene geometries. Our findings reveal that the symmetry of the stacking configurations plays a crucial role in determining the electronic band structure and the features of the Dirac cone crossings. HSSs exhibit distinct patterns of Dirac cone crossings, while LSSs show reduced symmetry and fewer crossings. We employ the Euler characteristic as a topological invariant to effectively capture the topological transitions in the Fermi surface, distinguishing between different stacking configurations. In particular, the Euler characteristic changes as the layers slide, providing a robust indicator of topological transitions in several cases. We also observe that the formation of Dirac nodes is highly dependent on the irreducible representations of the bands, which are linked to the underlying symmetry and energetic properties of the stackings. This dependence highlights the intricate relationship between symmetry, band topology, and electronic properties in BPN bilayers. The ability to tune the topological properties of BPN bilayers via sliding offers a promising route for controlling the electronic behavior in nanoscale devices. This tunability, combined with the unique electronic properties of BPN, highlights it as a potential candidate for applications in nanoelectronics and quantum computing.

Data availability statement

All data that support the findings of this study are included within the article (and any supplementary files).

Sliding Biphenylene Suppl available at https://doi.org/10.1088/2053-1583/ae2522/data1.

Acknowledgments

The authors thank the INCT de Nanomateriais de Carbono for providing support on the computational infrastructure. LLL thanks the CNPq scholarship. AL thanks the FAPERJ under Grant E-26/200.569/2023. LC acknowledges financial support from the Agencia Estatal de Investigación of Spain under Grant PID2022-136285NB-C31, and from Grant (MAD2D-CM)–(UCM5), Recovery, Transformation and Resilience Plan, funded by the European Union—NextGenerationEU. OAG acknowledges funding from European Union NextGenerationEU/PRTR project Consolidación Investigadora CNS2022-136025.

Author statement

L.L.Lage: Conceptualization, Calculations, Writing, Reviewing and Editing. S.Bravo: Investigation, Methodology, Calculations, Writing. O.Arroyo-Gascón: Investigation, Methodology, Calculations, and Reviewing. L.Chico: Conceptualization, Investigation, Writing, Reviewing, Supervision. A.Latgé: Conceptualization, Investigation, Writing, Reviewing, Supervision.

Conflict of interest

The authors declare that they have no known competing financial interests or personal relationships that could have appeared to influence the work reported in this paper.

Appendix. Tight-binding (TB) formulation

A TB parameterization is presented and compared with the DFT results. Our main goal is to examine the electrical characteristics of the bilayer structures for energies close to the Fermi level with low computational cost. Since the biphenylene structure is composed of simple sp^2 carbon bonds [3], a single p_z orbital TB Hamiltonian is adopted, to describe the different stackings, given by

$$H = \sum_{i,a} \varepsilon_i^a c_i^{\dagger a} c_i^a + \sum_{\substack{i,j \\ a}} t_{ij}^a c_i^{\dagger a} c_j^a + \sum_{\substack{i,j \\ a \neq b}} t_{ij}^{\perp ab} c_i^{\dagger a} c_j^b + h.c. \ , \tag{A.1}$$

where ε_i^a is the onsite energy of the atom located at the i site in the layer a, and $c_i^{a\dagger}$ (c_i^a) creates (annihilates) an electron at site i and layer a. The second term describes the intralayer couplings, t_{ij}^a being the corresponding hopping energies within the layer a. Clearly, for monolayers $a = 1$, the third summation is omitted. For bilayers, $a(b) = 1, 2$, and interlayer interactions, $t_{ij}^{\perp ab}$, depend on the stacking configuration between the top and bottom biphenylene layers. A suitable hopping parameterization is given by an intralayer hopping energy described by a decaying exponential function [9],

$$t_{ij}^a = t_1 \mathrm{e}^{-\beta\left(\frac{r_{ij}}{d_1}-1\right)} \ , \tag{A.2}$$

with r_{ij} being the distance between i, j lattice sites, t_1 the hopping related to the first nearest-neighbor distance d_1, and β a fitting parameter that controls the range of the interaction. As the ratio r_{ij}/d_1 is always larger than one beyond the first nearest neighbors, small β values allow one to increase the number of neighbors with non-negligible hoppings in the description.

For interlayer connection, we have also considered a decaying exponential function for the hopping energies given by $t_{ij}^{\perp ab} = t_0 \mathrm{e}^{-\alpha\left(\frac{r_{ij}}{d_\perp}-1\right)}$ with $d_\perp = 3.56$ Å the smallest interlayer distance and t_0 the hopping value in direct stacking, when two carbon atoms are exactly one above the other. The parameter α modulates the hopping strength between layers with increasing distance. The adopted TB parameterization is chosen by comparing the results with DFT calculations: $t_1 = -3.3$ eV, $t_0 = -0.33$ eV, $\beta = 2.2$, $\alpha = 1.47$. The onsite energy values are grouped into two sets: the four sites at the lateral corners of the hexagon and the two at the top and bottom vertices, given by $\epsilon_1 = -1.8$ eV and $\epsilon = -2.2$ eV, respectively.

DFT and TB results of different stacking configurations are shown in figures A1(a)–(d). Panels (a) and (b) correspond to two HSS, while panels (c) and (d) present two LSS cases. Each panel shows the band structures calculated with DFT (dark dots) and TB (continuous lines) along the high-symmetry path, with different behaviors at the type-II Dirac cones. The lower left figure of each panel presents an energy TB contour plot calculated at the energy of the first Dirac crossing (or anticrossing), next to the Γ point. The lower right figure of the panel shows a 2D rendering of the bands along with the constant

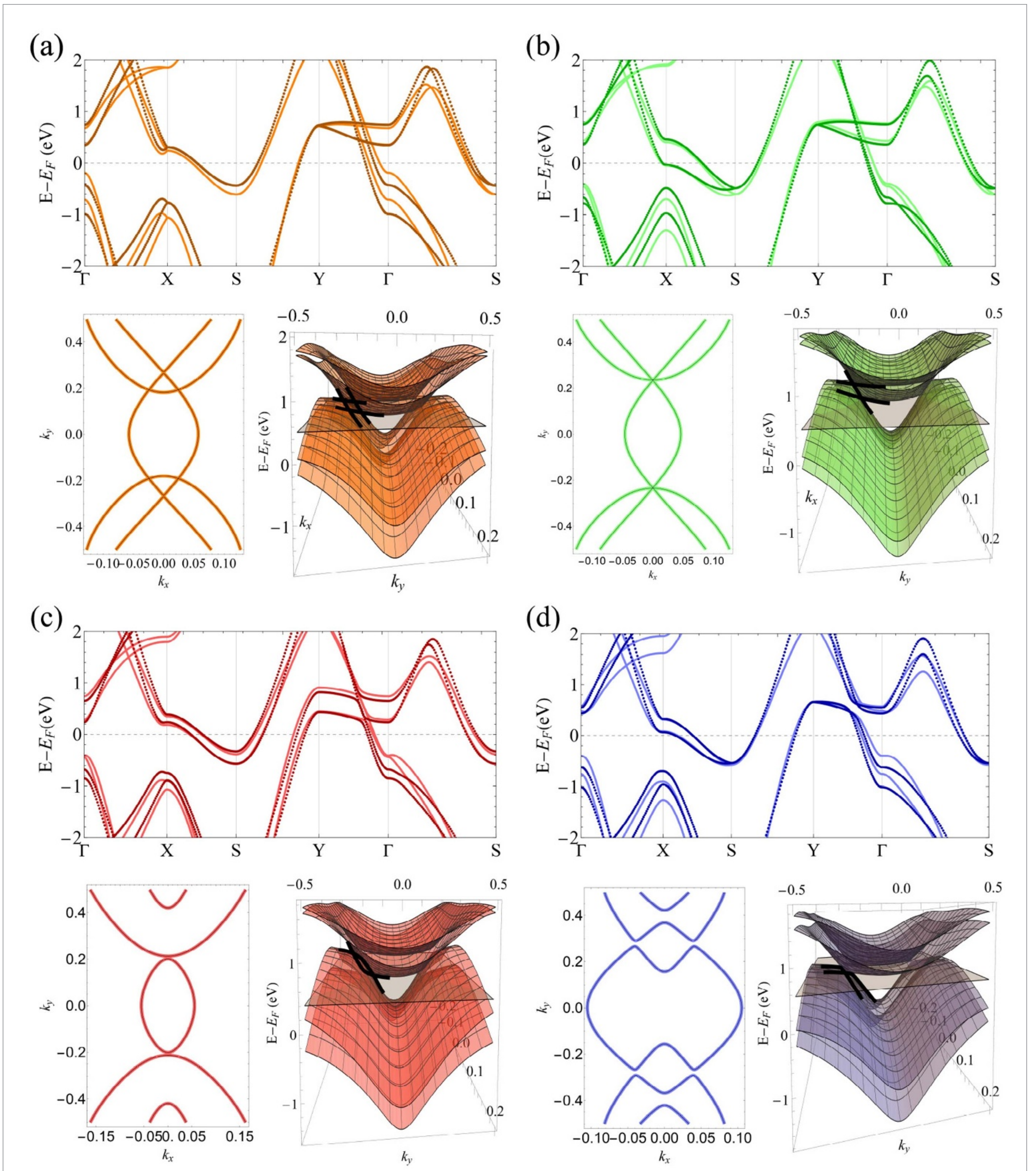

Figure A1. DFT (darker dots) and TB (solid lines) electronic bands for different bilayer stackings, TB energy contours evaluated at the first cone crossing and the respective surface cone plot for the stackings (a)–(b) HSS $(0.5, 0.5)$ and $(0.0, 0.5)$, and (c)–(d) LSS $(0.4, 0.0)$ and $(0.3, 0.5)$, respectively.

energy plane (in shaded gray) corresponding to the energy of the contour plot displayed in the bottom left part.

Different crossing and anticrossing features are observed. The contour plots corresponding to the HSS shown in figures A1(a) and (b), which belong to the $(0.5, 0.5)$ and $(0.0, 0.5)$ stackings respectively, have two crossings and one tiny anticrossing at each type-II Dirac cone. Figures A1(c) and (d), showing the results for LSS $(0.4, 0.0)$ and $(0.3, 0.5)$, respectively, reveal complete anticrossings between the contour lines.

ORCID iDs

L L Lage 0000-0002-9085-0388
S Bravo 0000-0001-5165-7916
O Arroyo-Gascón 0000-0003-2065-8398
Leonor Chico 0000-0002-7131-1266
Andrea Latgé 0000-0002-8152-6455

References

[1] Balaban A T 1989 Carbon and its nets *Comput. Math. Appl.* **17** 397–416

[2] Hudspeth M A, Whitman B W, Barone V and Peralta J E 2010 Electronic properties of the biphenylene sheet and its one-dimensional derivatives *ACS Nano* **4** 4565–70

[3] Fan Q *et al* 2021 Biphenylene network: a nonbenzenoid carbon allotrope *Science* **372** 852–6

[4] Niu K, Fan Q, Chi L, Rosen J, Gottfried J M and Björk J 2023 Unveiling the formation mechanism of the biphenylene network *Nanoscale Horiz.* **8** 368–76

[5] Girão E C, Macmillan A and Meunier V 2023 Classification of sp^2-bonded carbon allotropes in two dimensions *Carbon* **203** 611–9

[6] Kuritza D P, Miwa R H and Padilha J E 2024 Directional dependence of the electronic and transport properties of biphenylene under strain conditions *Phys. Chem. Chem. Phys.* **26** 12142–9

[7] Liu P-F, Li J, Zhang C, Tu X H, Zhang J, Zhang P, Wang B-T and Singh D J 2021 Type-II Dirac cones and electron-phonon interaction in monolayer biphenylene from first-principles calculations *Phys. Rev. B* **104** 235422

[8] Bafekry A, Faraji M, Fadlallah M M, Jappor H R, Karbasizadeh S, Ghergherehchi M and Gogova D 2022 Biphenylene monolayer as a two-dimensional nonbenzenoid carbon allotrope: a first-principles study *J. Phys.: Condens. Matter.* **34** 015001

[9] Lage L L, Arroyo-Gascón O, Chico L and Latgé A 2024 Robustness of type-II Dirac cones in biphenylene: from nanoribbons to symmetric bilayer stacking *Phys. Rev. B* **110** 165423

[10] Castro E V, Novoselov K S, Morozov S V, Peres N M R, Lopes dos Santos J M B, Nilsson J, Guinea F, Geim A K and Neto A H C 2007 Biased bilayer graphene: semiconductor with a gap tunable by the electric field effect *Phys. Rev. Lett.* **99** 216802

[11] McCann E, Abergel D and Fal'ko V 2007 The low energy electronic band structure of bilayer graphene *Eur. Phys. J. Spec. Top.* **148** 91–103

[12] Son Y-W, Jin H and Kim S 2022 Magnetic ordering, anomalous lifshitz transition and topological grain boundaries in two-dimensional biphenylene network *Nano Lett.* **22** 3112–7

[13] Lifshitz I M 1960 Anomalies of electron characteristics in the high pressure region *Zhur. Eksptl'. i Teoret. Fiz.* **38** (available at: www.osti.gov/biblio/4173345)

[14] Volovik G E 2017 Topological Lifshitz transitions *Low Temp. Phys.* **43** 47–55

[15] Galeski S *et al* 2022 Signatures of a magnetic-field-induced Lifshitz transition in the ultra-quantum limit of the topological semimetal $ZrTe_5$ *Nat. Commun.* **13** 7418

[16] Varlet A, Mucha-Kruczyński M, Bischoff D, Simonet P, Taniguchi T, Watanabe K, Fal'ko V, Ihn T and Ensslin K 2015 Tunable Fermi surface topology and lifshitz transition in bilayer graphene *Synth. Met.* **210** 19–31

[17] Aygar A M, Durnan O, Molavi B, Bovey S N R, Grüneis A and Szkopek T 2024 Mass inversion at the Lifshitz transition in monolayer graphene by diffusive, high-density, on-chip doping *ACS Nano* **18** 9092–9

[18] Pletikosić I, Gu G D and Valla T 2014 Inducing a lifshitz transition by extrinsic doping of surface bands in the topological crystalline insulator $Pb_{1-x}Sn_xSe$ *Phys. Rev. Lett* **112** 146403

[19] Chi Z *et al* 2024 Pressure-induced lifshitz transition in the type-II Weyl semimetal WP2 *Mater. Today Phys.* **42** 101372

[20] Krivenkov M, Marchenko D, Golias E, Sajedi M, Frolov A S, Sánchez-Barriga J, Fedorov A, Yashina L V, Rader O and Varykhalov A 2023 Lifshitz transition in titanium carbide driven by a graphene overlayer *Phys. Rev. Res.* **5** 023120

[21] Son Y-W, Choi S-M, Hong Y P, Woo S and Jhi S-H 2011 Electronic topological transition in sliding bilayer graphene *Phys. Rev. B* **84** 155410

[22] Gavensky P, Usaj L and Balseiro G C A 2016 Photo-electrons unveil topological transitions in graphene-like systems *Sci. Rep.* **6** 36577

[23] Jayaraman A, Hsieh K, Ghawri B, Mahapatra P S, Watanabe K, Taniguchi T and Ghosh A 2021 Evidence of Lifshitz transition in the thermoelectric power of ultrahigh-mobility bilayer graphene *Nano Lett.* **21** 1221–7

[24] Bhattacharyya S and Singh A K 2016 Lifshitz transition and modulation of electronic and transport properties of bilayer graphene by sliding and applied normal compressive strain *Carbon* **99** 432–8

[25] Andrei E Y, Efetov D K, Jarillo-Herrero P, MacDonald A H, Mak K F, Senthil T, Tutuc E, Yazdani A and Young A F 2021 The marvels of moiré materials *Nat. Rev. Mater.* **6** 201–6

[26] Fujimoto M and Koshino M 2021 Moiré edge states in twisted bilayer graphene and their topological relation to quantum pumping *Phys. Rev. B* **103** 155410

[27] Li Y, Eaton A, Fertig H A and Seradjeh B 2022 Dirac magic and Lifshitz transitions in AA-stacked twisted multilayer graphene *Phys. Rev. Lett.* **128** 026404

[28] Ribeiro-Palau R, Zhang C, Watanabe K, Taniguchi T, Hone J and Dean C R 2018 Twistable electronics with dynamically rotatable heterostructures *Science* **361** 690–3

[29] Sui F, Jin M, Zhang Y, Qi R, Wu Y-N, Huang R, Yue F and Chu J 2023 Sliding ferroelectricity in van der Waals layered γ-InSe semiconductor *Nat. Commun.* **14** 36

[30] Yasuda K, Zalys-Geller E, Wang X, Bennett D, Cheema S S, Watanabe K, Taniguchi T, Kaxiras E, Jarillo-Herrero P and Ashoori R 2024 Ultrafast high-endurance memory based on sliding ferroelectrics *Science* **385** 53–56

[31] Michetti P and Recher P 2011 Spintronics devices from bilayer graphene in contact to ferromagnetic insulators *Phys. Rev. B* **84** 125438

[32] Alcón I, Calogero G, Papior N, Antidormi A, Song K, Cummings A W, Brandbyge M and Roche S 2022 Unveiling the multiradical character of the biphenylene network and its anisotropic charge transport *J. Am. Chem. Soc.* **144** 8278–85

[33] López-Alcalá D and Baldoví J J 2025 Magnetic proximity effect in biphenylene monolayer from first-principles *J. Mater. Chem. C* **13** 5993–9

[34] Xu H *et al* 2020 High spin Hall conductivity in large-area type-II Dirac semimetal $PtTe_2$ *Adv. Mater.* **32** 2000513

[35] Li P, Zhang C, Wen Y, Cheng L, Nichols G, Cory D G, Miao G-X and Zhang X-X 2019 Anisotropic planar Hall effect in the type-II topological Weyl semimetal wte_2 *Phys. Rev. B* **100** 205128

[36] Gadelha A C *et al* 2021 Localization of lattice dynamics in low-angle twisted bilayer graphene *Nature* **590** 405–9

[37] Pan J *et al* 2025 Topological valley transport in bilayer graphene induced by interlayer sliding *Phys. Rev. Lett.* **135** 126603

[38] Stern M V, Waschitz Y, Cao W, Nevo I, Watanabe K, Taniguchi T, Sela E, Urbakh M, Hod O and Shalom M B 2021 Interfacial ferroelectricity by van der Waals sliding *Science* **372** 1462–6

[39] Zhang Q, Fan A, Wang Y, Wu F, Li L, Meng H and Geng D 2025 Emerging frontiers in two-dimensional sliding ferroelectrics npj 2D *Mater. Appl.* **9** 76

[40] Yasuda K, Wang X, Watanabe K, Taniguchi T and Jarillo-Herrero P 2021 Stacking-engineered ferroelectricity in bilayer boron nitride *Science* **372** 1458–62

[41] Wang J, Cheng F, Sun Y, Xu H and Cao L 2024 Stacking engineering in layered homostructures: transitioning from 2D to 3D architectures *Phys. Chem. Chem. Phys.* **26** 7988–8012

[42] Soluyanov A A, Gresch D, Wang Z, Wu Q, Troyer M, Dai X and Bernevig B A 2015 Type-II Weyl semimetals *Nature* **527** 495–8

[43] Muechler L, Alexandradinata A, Neupert T and Car R 2016 Topological nonsymmorphic metals from band inversion *Phys. Rev. X* **6** 041069

[44] Yang H F *et al* 2019 Topological Lifshitz transitions and Fermi arc manipulation in Weyl semimetal NbAs *Nat. Commun.* **10** 3478

[45] Lin C *et al* 2021 Visualization of the strain-induced topological phase transition in a quasi-one-dimensional superconductor $TaSe_3$ *Nat. Mater.* **20** 1093–9

[46] Mori R, Marshall P B, Ahadi K, Denlinger J D, Stemmer S and Lanzara A 2019 Controlling a Van Hove singularity and Fermi surface topology at a complex oxide heterostructure interface *Nat. Commun.* **10** 5534

[47] Dan S, Kargeti K, Sahoo R C, Dan S, Pal D, Verma S, Chakravarty S, Panda S K and Patil S 2023 Magnetotransport properties and Fermi surface topology of the nodal line semimetal InBi *Phys. Rev. B* **107** 205111

[48] He P, Hsu C-H, Shi S, Cai K, Wang J, Wang Q, Eda G, Lin H, Pereira V M and Yang H 2019 Nonlinear magnetotransport shaped by Fermi surface topology and convexity *Nat. Commun.* **10** 1290

[49] Wang D *et al* 2023 Twisted bilayer zigzag-graphene nanoribbon junctions with tunable edge states *Nat. Commun.* **14** 1018

[50] Tam P M, Claassen M and Kane C L 2022 Topological multipartite entanglement in a Fermi liquid *Phys. Rev. X* **12** 031022

[51] Giannozzi P *et al* 2009 QUANTUM ESPRESSO: a modular and open-source software project for quantum simulations of materials *J. Phys.: Condens. Matter* **21** 395502

[52] Giannozzi P *et al* 2017 Advanced capabilities for materials modelling with quantum ESPRESSO *J. Phys.: Condens. Matter* **29** 465901

[53] Perdew J P, Burke K and Ernzerhof M 1996 Generalized gradient approximation made simple *Phys. Rev. Lett.* **77** 3865–8

[54] van Setten M, Giantomassi M, Bousquet E, Verstraete M, Hamann D, Gonze X and Rignanese G-M 2018 The pseudoDojo: training and grading a 85 element optimized norm-conserving pseudopotential table *Comput. Phys. Commun.* **226** 39–54

[55] Grimme S, Antony J, Ehrlich S and Krieg H 2010 A consistent and accurate *ab initio* parametrization of density functional dispersion correction (DFT-D) for the 94 elements H-Pu *J. Chem. Phys.* **132** 154104

[56] Togo A, Chaput L, Tadano T and Tanaka I 2023 Implementation strategies in phonopy and phono3py *J. Phys.: Condens. Matter* **35** 353001

[57] Supplementary Material link. Tight-binding and density functional theory calculations and discussion.

[58] Madsen G K, Carrete J and Verstraete M J 2018 Boltztrap2, a program for interpolating band structures and calculating semi-classical transport coefficients *Comput. Phys. Commun.* **231** 140–5

[59] Iraola M, Mañes J L, Bradlyn B, Horton M K, Neupert T, Vergniory M G and Tsirkin S S 2022 Irrep: symmetry eigenvalues and irreducible representations of *ab initio* band structures *Comput. Phys. Commun.* **272** 108226

[60] Chowdhury S, Ghosal S, Mondal D and Jana D 2022 First-principles and machine-learning study of electronic and phonon transport in carbon-based aa-stacked bilayer biphenylene nanosheets *J. Phys. Chem. Solids* **170** 110909

[61] Dresselhaus M S, Dresselhaus G and Jorio A 2008 *Group Theory: Application to the Physics of Condensed Matter* (Springer)

[62] Aroyo M I, Perez-Mato J M, Capillas C, Kroumova E, Ivantchev S, Madariaga G, Kirov A and Wondratschek H 2006 Bilbao crystallographic server: I. Databases and crystallographic computing programs *Z. Kristallogr.* **221** 15–27

[63] Aroyo M I, Kirov A, Capillas C, Perez-Mato J M and Wondratschek H 2006 Bilbao crystallographic server. II. Representations of crystallographic point groups and space groups *Acta Crystallogr. A* **62** 115–28

[64] Nakahara M 2018 *Geometry, Topology and Physics* (CRC press)

[65] Tam P M, De Beule C and Kane C L 2023 Topological andreev rectification *Phys. Rev. B* **107** 245422

[66] Zhang C *et al* 2025 Zero-field chiral edge transport in an intrinsic magnetic topological insulator $MnBi_2Te_4$ *Nat. Commun.* **16** 5587

[67] Chang C-Z, Zhang J, Feng X, Shen J and Zhang Z 2013 Experimental observation of the quantum anomalous Hall effect in a magnetic topological insulator *Science* **340** 167–70

[68] Tam P M and Kane C L 2023 Probing Fermi sea topology by andreev state transport *Phys. Rev. Lett.* **130** 096301

[69] Kane C L 2022 Quantized nonlinear conductance in ballistic metals *Phys. Rev. Lett.* **128** 076801